ISSN 1063-7710, Acoustical Physics, 2023, Vol. 69, No. 4, pp. 459–470. © Pleiades Publishing, Ltd., 2023.

NONLINEAR ACOUSTICS

Nonlinear Ultrasound Fields Generated by an Annular Array with Electronic and Geometric Adjustment of its Focusing Angle

E. M. Ponomarchuk[a, *], P. V. Yuldashev[a], D. A. Nikolaev[a], S. A. Tsysar[a], A. A. Mironova[a], and V. A. Khokhlova[a, **]

[a] *Faculty of Physics, Moscow State University, Moscow, 119991 Russia*

**e-mail: ponomarchuk.em14@physics.msu.ru*

***e-mail: vera@acs366.phys.msu.ru*

Received May 29, 2023; revised June 8, 2023; accepted June 19, 2023

Abstract—Linear and nonlinear fields produced by a twelve-ring annular array with varied axial electronic focus steering distances and varied number of activated elements were simulated using wide-angle parabolic representation of the Westervelt equation. The effects of electronic adjustment of the focusing angle and/or switching off the array elements were investigated with regard to the shock-forming conditions at the focus and in the grating lobes in water. Prefocal steering was shown to result in shock formation in the postfocal grating lobe, which can occur at lower array power than that required for shock formation at the main focus. Postfocal steering resulted in shock formation at the main focus and no shock in the prefocal grating lobe at any power considered. To decrease focusing angle, switching off the outer rings was more favorable than postfocal steering with all rings enabled: a fully developed shock of the same amplitude formed at the same source pressure amplitude but with lower pressure level in the prefocal grating lobe. To increase focusing angle, prefocal steering with the outer rings switched off was less favorable than using all array elements with no steering: higher source pressure amplitude was required for a fully developed shock formation at the focus, with additional shock fronts forming in the postfocal grating lobe.

Keywords: high-intensity focused ultrasound, shock waves, nonlinear effects, annular phased array, electronic focus steering, wide-angle parabolic equation

DOI: 10.1134/S1063771023600560

INTRODUCTION

A rapidly increasing worldwide interest in the use of high-intensity focused ultrasound (HIFU) for noninvasive therapeutic and surgical applications, from hyperthermia and thermal ablation therapies already used in clinical practice [1–3] to newer mechanical ablation techniques such as histotripsy [4–7], has sparked a lot of research in both acoustics and bioengineering. For such newer applications to be feasible, specified high acoustic pressure levels need to be reached or shock fronts of certain amplitudes need to be formed at the focus. New biomedical technologies based on acoustic radiation force can also benefit from utilizing high pressures and corresponding nonlinear effects [8, 9]. Achievable pressures in both linear and nonlinear ultrasound fields are primarily determined by the transducer focusing angle [10–12], or, in other words, by its F-number (F#) defined as a ratio of the transducer focal distance to its aperture. Stronger-focusing transducers (i.e., with larger focusing angles, or lower F-numbers) are typically capable of producing higher focal pressure levels and shock front amplitudes but require higher acoustic power driving the transducer to achieve a shock-forming regime. Using transducers with different focusing angles, therefore, makes it possible to control focal pressure and shock amplitude level required for each specific medical application. As an alternative, the use of multi-element phased arrays allows for dynamic focusing by introducing phase delays to the elements required to steer the focus to the targeted point [13–15]. Hence, axial electronic steering of the focus can also adjust the focusing angle and control the achievable pressure levels. A common disadvantage of phased arrays, however, is formation of unwanted grating lobes in the produced acoustic fields that, given sufficient intensity, can lead to damage of tissues outside of the targeted region [13, 15].

Several multi-element arrays operating in nonlinear regimes have been previously numerically characterized for thermal [16, 17] and mechanical [18] HIFU applications. Focal pressure amplitudes were shown to reach a maximum at a certain prefocal steering distance, but otherwise decrease with focus axial shift [18]. Prefocal axial steering was shown to require higher source voltages to reach shock-forming conditions at the steered focus and resulted in higher shock amplitude [18]. This agrees with the patterns reported in [12] for stronger-focusing single-element transducers as both larger focusing angle and the drop in focal pressure due to steering contributed to the required power increase. On the contrary, postfocal steering required about the same source voltage to reach shock-forming conditions at the focus as compared to the no steering case, while less power is typically required for less focused single-element transduces [18]. This is attributed to a combination of the decrease of the focusing angle and the drop in pressure due to steering. Postfocal focus steering also resulted in formation of a prefocal grating lobe shifting closer to the steered focus and increasing in amplitude with axial steering distance [16]. Possible nonlinear effects in the grating lobe still require careful consideration as they may lead to formation of shocks outside of the targeted focal region and, hence, result in unwanted damage to any structures present there.

As an alternative to electronic adjustment, the focusing angle of annular axially symmetric arrays can also be changed by switching on and off the outer array elements, thus varying the effective aperture and geometrically adjusting the angle. The two abovementioned approaches to adjust the focusing angle using multi-element arrays (i.e., electronic focus steering or switching on and off the elements) are essentially different and require comparative analysis of linear and nonlinear effects they introduce.

The goal of this work was, therefore, to compare the effects of electronic *vs* geometric adjustment of the focusing angle on the parameters of linear and nonlinear acoustic fields. A 12-ring annular phased array, previously described in [19] and used experimentally in [20], was considered as an example. Numerical modeling of the array fields was performed based on the wide-angle parabolic representation of the Westervelt equation [21–23].

1. NUMERICAL MODELING METHODS

An array model that imitates a 2 MHz 12-element piezocomposite annular focused transducer (Imasonic, France) was considered in order to set boundary conditions for acoustic simulations [19]. The array had a shape of a concave spherical bowl with 80 mm radius of curvature, 100 mm aperture, and 40 mm diameter of the central opening (Fig. 1a). The active area of the array comprised twelve annular elements of equal area, 0.5 mm spacing between the elements, and uniform vibrational velocity distribution.

Ultrasound fields generated using various configurations of the array were simulated using the "HIFU beam" software, which allows for modeling nonlinear axially symmetric focused ultrasound fields containing shock fronts based on the wide-angle parabolic representation of the Westervelt equation [21–23]. The software was developed at the Laboratory for industrial and medical ultrasound of Lomonosov Moscow State University and is freely available for download [24]. The "HIFU beam" graphical interface allowed for switching off specific rings of the array by zeroing their vibrational velocity amplitude, as well as for electronic steering of the focus by automatically calculating the required phases based on the delays of the signals traveling from the centers of each ring defined as a half-sum of their inner and outer zenith angles to the focus. The fields were calculated in a 2-D spatial window with [0; 160] mm axial range equal to two focal distances and [−100; 100] mm radial range, with 0.05 and 0.025 mm axial and radial grid steps, respectively. All simulations were performed in water with acoustic parameters characteristic for 19°C: speed of sound $c = 1479.2$ m/s, density $\rho = 997.8$ kg/m^3, nonlinear coefficient $\beta = 3.5$, diffusivity of sound $\delta = 4.33$ mm^2/s [25].

1.1. Acoustic Model Validation

To validate the accuracy of the proposed simulation approach based on the wide-angle approximation of diffraction effects and an assumption of uniformly vibrating surface of the transducer used to set boundary conditions, linear fields of the array with no focus steering were simulated using the "HIFU beam" software, calculated analytically based on the Rayleigh integral formula for a spherical cup [26, 27], and compared to the experimental data obtained previously using acoustic holography measurements [19]. Both "HIFU beam" simulations and analytical calculations were performed for uniform distribution of the vibrational velocity amplitude u_0 on the array surface (Fig. 1a), as opposed to the actual non-uniform velocity distribution of the existing array reconstructed from the measured acoustic hologram (Fig. 1b, [19]).

Analytical solutions for the axial pressure distribution and the transverse pressure distribution in the focal plane of the array were derived from the Rayleigh's solution for a spherical concave radiator using superposition of the fields of the array elements [26]:

$$p(z) = \sum_{m=1}^{12} \left\{ -\frac{2i\rho c u_0}{1-\dfrac{z}{F}} \exp\left(i\frac{k}{2}\left(L_m^{\max} + L_m^{\min}\right)\right) \sin\left(\frac{k}{2}\left(L_m^{\max} - L_m^{\min}\right)\right) \right\}, \tag{1}$$

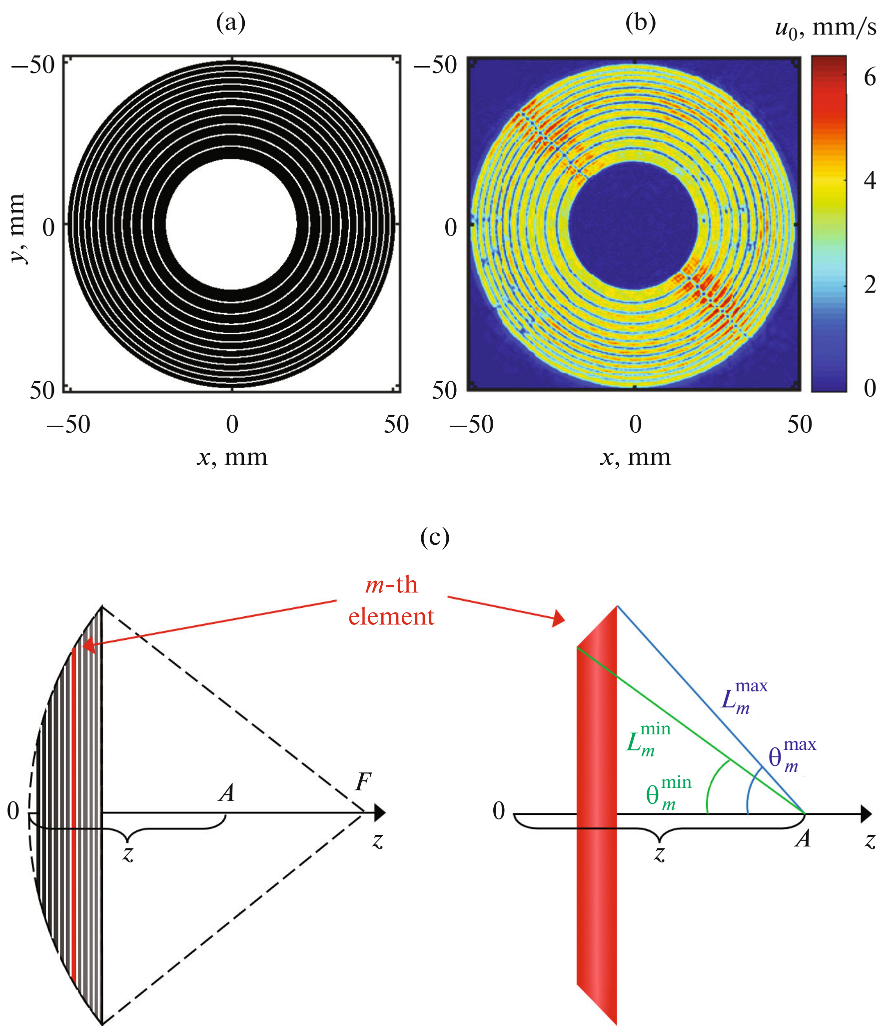

Fig. 1. Illustration of the considered array model. (a) Front view schematics of the array. (b) Amplitude distribution of the normal component of vibrational velocity on the array surface reconstructed from the hologram measured with no focus steering [19]. (c) Schematics of the array parameters used in analytical calculations, Eqs. (1)–(2).

$$p(r) = \sum_{m=1}^{12} p_m(r),$$
$$p_m(r) = \frac{i\rho c u_0 F e^{-ikF}}{r} \tag{2}$$
$$\times \left\{ J_1\left(kr\sin\theta_m^{max}\right)\sin\theta_m^{max} - J_1\left(kr\sin\theta_m^{min}\right)\sin\theta_m^{min} \right\}.$$

Here c is the sound speed, ρ—water density, c—sound speed in water, u_0—amplitude of the normal component of vibrational velocity on the array surface, $k = \omega/c$—wavenumber, ω—angular frequency, F—focal distance, L_m^{max} and L_m^{min}—distances from the current axial point z to the outer and inner boundary of the m-th element, θ_m^{min} and θ_m^{max} are the inner and outer zenith angles of the m-th element (Fig. 1c), $J_1(\cdot)$ is Bessel function of the first kind.

Acoustic field generated by an existing array was calculated using the Rayleigh integral with boundary condition reconstructed from acoustic holography measurements [19].

Pressure amplitude distributions on the array axis and transversely in the focal plane obtained using "HIFU beam" simulations, analytical solution, and holography data, were then compared to validate the acoustic model for further nonlinear simulations.

1.2. Electronic Focus Steering

To investigate the effect of electronic focus steering on acoustic field of the array, first, linear calculations were performed for the twelve- and ten-ring arrays when focusing at varied steering distances, starting from the geometric focus and proceeding with 0.1 mm step for up to 25 mm towards or away from the array. The focusing gain in the main lobe and ratio of pressure amplitudes in the grating lobe *vs* the main lobe were calculated for each focusing configuration to determine the effective and safe steering ranges. The safe range was defined according to the commonly accepted criterion used in thermal HIFU applications: the maximum intensity in any grating lobe must be below 10% of the maximum intensity in the main lobe (i.e., below 31.6% in terms of the pressure amplitude) [13, 28]. Such safe steering limits will be further referred to as "thermally safe" limits. For the nonlinear ultrasound applications, however, this criterion can be softened since such applications typically rely not on the intensity, but on the amplitude of a shock front that forms at the focus due to the nonlinear propagation effects [4–7]. Shock formation is highly dependent on the pressure level and, therefore, the shock forms first in the main lobe, whereas no shock is yet present in the lower-amplitude grating lobes. The effective steering is typically introduced within the range, where the linear pressure amplitude at the steered focus drops by no more than 10–20% compared to the maximum achievable pressure, as this drop can typically be compensated by voltage increase [18, 29]. Here we considered the effective range defined at 10% drop from the maximum pressure obtained with no steering (about 15% of the maximum achievable pressure). Such steering limits will be further referred to as "10%-pressure drop" limits. These initial linear simulations allowed to determine the safe and effective steering ranges for the arrays, as well as to characterize their fields through linear focusing gain G (the ratio of pressure amplitudes at the focus and at the array surface), and axial (δz) and transversal (δr) dimensions of the main focal lobe at –6 dB and zero pressure levels.

Then, nonlinear acoustic fields were simulated at increasing source pressure amplitudes $p_0 = \rho c u_0$ up to $p_0 = 0.65$ MPa with the focus positioned within the steering limits. Nonlinear distortion of the pressure waveforms in the main and grating lobes were analyzed depending on the source pressure amplitude, and saturation curves for the peak positive $p+$ and negative $p-$ pressures, as well as for the shock amplitudes A_s were obtained. The shock amplitude A_s was determined as the pressure change between the time points at which the time derivative of pressure decreased to 0.025 of its peak value, given the time points were less than 0.006 μs apart [11, 30, 31]. The source pressure amplitude p_0^{dev} and the output power W_0^{dev} required for the formation of a fully developed shock (A_s^{dev}) were determined for each field geometry. A fully developed shock regime was defined as the level of distortion with maximum ratio of the shock amplitude to the source pressure amplitude $A_s/p_0 = (A_s/p_0)_{max}$, which is also characterized by the shock amplitude being equal to the peak positive pressure [11].

1.3. Decreasing Focusing Angle: Electronic vs Geometric

To study the effect of decreasing the focusing angle using electronic *vs* geometric approaches, a fixed focusing angle of 71° was achieved using two configurations of the array. Electronic approach involved operation of the full array and postfocal electronic focus steering to $\Delta z = +7.5$ mm. Geometric approach involved switching off the two outer rings of the array with no focus steering. Similar to procedures described in section 1.2, linear focusing gain and dimensions of the main focal lobe were compared for the two configurations. Nonlinear simulations were then performed at increasing source pressure amplitudes p_0. Distortion of the pressure waveforms in the main and grating lobes were analyzed and saturation curves for the peak positive pressure $p+$, peak negative pressure $p-$, and shock front amplitude A_s were compared. Characteristic source pressure amplitude p_0^{dev} and the output power W_0^{dev} required for formation of a fully developed shock at the focus and the corresponding shock amplitude (A_s^{dev}) were determined and compared for the two configurations.

1.4. Increasing Focusing Angle: Electronic vs Geometric

To study the effect of increasing the focusing angle using electronic *vs* geometric approaches, a fixed focusing angle of 77° was achieved using the following two configurations of the annular array. In the electronic approach, two outer rings of the array were switched off and the focus of the resulting ten-ring array was electronically shifted for $\Delta z = -7$ mm (i.e., prefocally). Geometric setting of the angle was achieved by enabling all rings of the array with no steering of the focus. Linear and nonlinear fields of the two configurations were analyzed and compared as described in section 1.3.

2. RESULTS AND DISCUSSION

2.1. Validation Results for Linear Acoustic Modeling

Figure 2 compares normalized linear pressure amplitude distributions obtained from holography measurements (points), analytical solution (black dashed line), and "HIFU beam" simulations (gray solid line) for the case of no focus steering. Experimental and analytical curves practically coincide suggesting that the field generated by uniformly vibrating array (Fig. 1a) accurately matches the field of the real array with non-uniform distribution of vibrational velocity on its surface (Fig. 1b). The results of "HIFU beam" field simulations agree very well with the analytical full-diffraction solution, thus confirming high accuracy of governing the diffraction effects using wide-angle parabolic approximation. The results also show that even without focus steering, a strong grating lobe forms prefocally with amplitude close to the safe

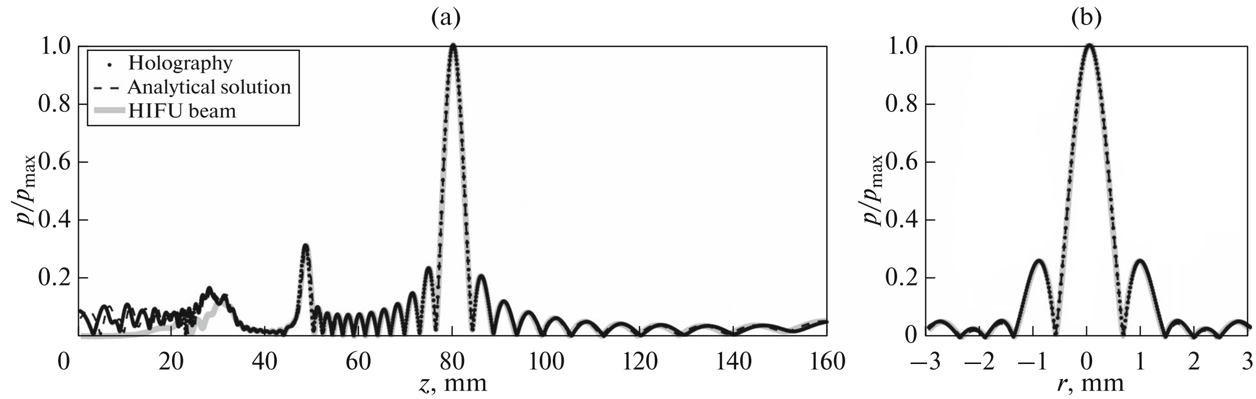

Fig. 2. Validation results for linear acoustic modeling. (a)—Normalized pressure amplitude distributions along the array axis and (b)—transversal in the focal plane obtained with no focus steering from holography measurements (points), analytical solution (black dashed line), and simulations in wide-angle parabolic approximation using "HIFU beam" software (gray solid line).

threshold of 31.6% from the pressure maximum in the main lobe.

Good agreement between the results obtained with the uniform boundary condition and wide-angle parabolic approximation of the diffraction effects for the strongly focused field of the array confirmed that the proposed approach can be used in further nonlinear field simulations. All numerically modeled array configurations and the corresponding characteristic parameters of the generated linear and nonlinear fields obtained from the simulations are summarized in Table 1.

2.2. Electronic Focus Steering Effects

Steering effects in linear array field. Figure 3 illustrates the effects occurring in the linear fields produced by the (I) twelve- and (II) ten-ring arrays when the focus was electronically steered prefocally or postfocally. No significant difference was observed for the two configurations, apart from a 17% lower focusing gain for the ten-ring array due to a 17% smaller active surface area having two outer rings switched off. Steering limits for both cases were found to be practically the same: thermally safe limits (solid blue and black curves in Fig. 3) were [–12.8; 0.14] mm and [–12.6; 0.3] mm for the twelve- and ten-ring arrays, respec-

Table 1. Summary of the modeled array configurations and the resulting characteristic field parameters. N—numbers of enabled elements, Δz—steering distance (positive in postfocal steering, negative in prefocal steering), φ—focusing angle, $F\#$ —F-number, S_{act}—active surface area, G—focusing gain, δz—linear focal lobe length between nulls and at –6 dB pressure level, δr—linear focal lobe width between nulls and at –6 dB pressure level, $p_0^{dev}\left(W_0^{dev}\right)$—source pressure amplitude (acoustic power) required for a fully developed shock formation in the main lobe, A_s^{dev}—fully developed shock amplitude in the main lobe

	Array configuration parameter					Linear field parameters			Fully developed shock		
	N	Δz, mm	φ	$F\#$	S_{act}, mm^2	G	$\delta z(0)/\delta z(-6\text{ dB})$, mm	$\delta r(0)/\delta r(-6\text{ dB})$, mm	p_0^{dev}, MPa	W_0^{dev}, W	A_0^{dev}, MPa
Electronic focus steering effects		–19.5	99°	0.6		96	5/3	1/0.6	0.675	964	237
		–12.8	89°	0.67		109	5.8/3.5	1.1/0.65	0.47	468	193
		0	77°	0.8		106	7.75/4.65	1.25/0.75	0.3	191	136
	12	+7.5	71°	0.88	6247	96	9.1/5.42	1.34/0.8	0.32	217	121
Decreasing focusing angle	12	+7.5		0.88	6247	96	9.1/5.42	1.34/0.8	0.32	217	121
	10	0	71°	0.86	5206	88	9.4/5.65	1.3/0.8	0.32	181	122
Increasing focusing angle	12	0		0.8	6247	106	7.75/4.65	1.25/0.75	0.3	191	136
	10	–7	77°	0.79	5206	93	8.05/4.8	1.2/0.75	0.4	282	148

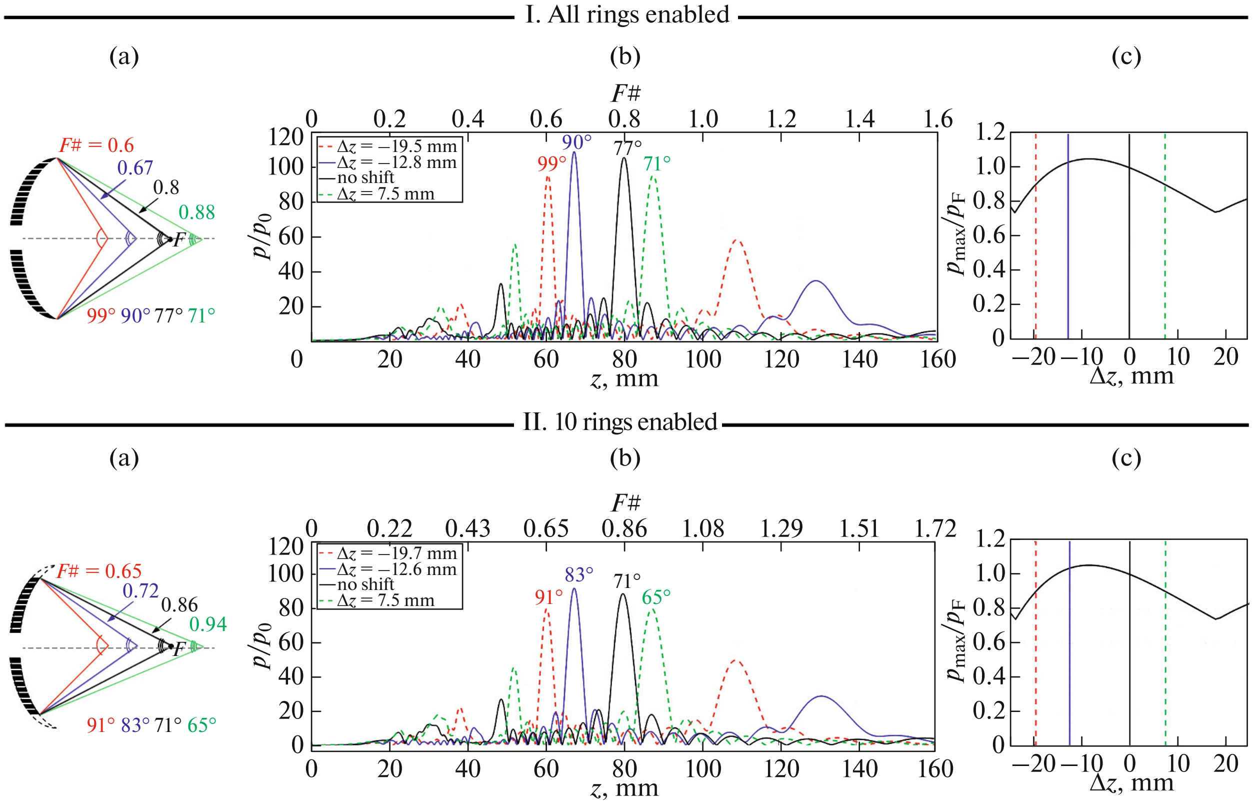

Fig. 3. Illustration of the focus steering effect on the linear field of the array with (I) all twelve rings enabled, (II) ten inner rings enabled. (a)—Schematics of varied electronically steered focus positions relative to the geometric focus *F*. (b)—Axial pressure amplitude distributions relative to the source pressure amplitude p_0 for varied steered focus locations. Solid lines represent thermally safe steering limits: prefocal (blue) and postfocal (black). Dashed lines represent 10%-pressure drop steering limits: prefocal (red) and postfocal (green). Corresponding effective *F*-numbers (*F*#) of the beams are indicated on the top horizontal axis. (c)—Ratio of the maximum pressure amplitude in the steered field (p_{max}) to the focal pressure without steering (p_F) as a function of steering distance Δz. Vertical lines represent steering limits from (a)–(b).

tively; 10%-pressure drop limits (dashed red and green curves in Fig. 3) were [–19.5; 7.5] and [–19.7; 7.5] mm. Prefocal steering beyond $\Delta z = -4$ mm resulted in formation of a postfocal grating lobe within the double focal distance range, which was increasing in amplitude and shifting closer to the main lobe as the focus steering distance increased (blue and red curves in Fig. 3). Similarly, postfocal steering (green curves in Fig. 3) increased the amplitude of the prefocal grating lobe, preexistent in the field with no focus steering (black curves in Fig. 3), and shifted it closer to the main lobe. Such behavior of the grating lobe is well-known and agrees with literature [16]. At the 10%-pressure drop limits, the pressure amplitudes in the grating lobe relative to that in the main lobe were also similar for both arrays: 61–62% with prefocal steering (red curves in Fig. 3) and 57–58% with postfocal steering (green curves in Fig. 3). The focusing gain reached a maximum when focusing prefocally, $\Delta z = -8.5$ mm, but otherwise decreased with increasing steering distance (Fig. 3c). The largest increase in the focusing gain was 5.1 and 5.3% as compared to that without steering for twelve- and ten-ring arrays, respectively. Such behavior of the pressure amplitude at the steered focus as a function of the steering distance is also well-known and agrees with literature [18]. When the focus was steered beyond $\Delta z = -24$ mm (prefocally) or $\Delta z = 18$ mm (postfocally), the pressure amplitude in the grating lobe exceeded that in the main lobe, which is indicated by the increasing ratio p_{max}/p_F of the maximum pressure in the array field (p_{max}) to the focal pressure without steering (p_F) shown in Fig. 3c. The dimensions of the focal lobe increased both axially and transversely with focus shifting away from the transducer, and decreased when shifting closer to the transducer (Table 1), in accordance with the stronger- or weaker focusing geometry of the beams [12, 18].

Prefocal steering effects in nonlinear array field. Fig. 4 illustrates the effects occurring in nonlinear fields of the twelve-ring array at the focus and in the grating lobe when the focus was electronically steered. In case of prefocal steering (Fig. 4, I) to the thermally safe ($\Delta z = -12.8$ mm, blue curves) and 10%-pressure drop (–19.5 mm, red curves) limits (Fig. 3, I), fully developed shock formed at the main focus (squares in

Fig. 4,Ib) at a higher source pressure (p_0^{dev} = 0.675 *vs* 0.47 MPa) and had a higher amplitude (A_s^{dev} = 237 *vs* 193 MPa) in the stronger-focusing case (red) as compared to the weaker-focusing case (blue) (Fig. 4,Ib; Table 1). These effects are typical for more focused beams [12] and additional decrease of the pressure due to electronic focus steering (Fig. 3,Ic) [18].

Nonlinear effects in the postfocal grating lobe relative to those in the main focus for the same steering configurations are illustrated in Fig. 4,Ic ($\Delta z = -12.8$ mm), and Fig. 4,Id ($\Delta z = -19.5$ mm). The ratio of the peak positive ($p+$, solid line) and negative ($p-$, dashed line) pressures in the grating lobe *vs* those in the main lobe, and shock amplitudes in the main lobe (A_s^{main}, x-symbols) and in the grating lobe (A_s^{grat}, circles) as functions of the source pressure amplitude p_0 are presented. The peak negative pressure in the grating lobe was lower than that in the main lobe for both steering cases and for all source pressure amplitudes p_0 (dashed curves in Fig. 4,Ic, 4,Id). Peak positive pressure in the grating lobe, however, for some output pressure levels of the array ($0.18 < p_0 < 0.36$ MPa), was higher than that in the main lobe by up to 55% when the focus was steered towards the array to the 10%-pressure drop limit at $\Delta z = -19.5$ mm (Fig. 4,Id). In this steering case, the maximum ratio of the peak positive pressure in the grating *vs* in the main lobe (triangle in Fig. 4,Id) corresponded to the onset of shock formation in the postfocal grating lobe (dashed red line in Fig. 4,Ie).

Figures 4,Ie, 4,If illustrate the nonlinear distortion of the waveforms in the main lobe (solid lines) *vs* in the grating lobe (dashed lines) for the same two steering configurations in two representative regimes: when the ratio of peak positive pressure in the grating *vs* main lobe reached its maximum (Fig. 4,Ie), and when a fully developed shock formed in the main lobe (Fig. 4,If). For both prefocal steering cases (blue and red), when the ratio of the peak positive pressure in the grating lobe to that in the main lobe reached its maximum (triangles in Fig. 4,Ic, 4,Id), the pressure waveform in the grating lobe (dashed curves in Fig. 4,Ie) were more nonlinearly distorted than that in the main focus (solid curves in Fig. 4,Ie). This, apparently, led to the shock formation in the grating lobe when the source pressure amplitude p_0 was further increased (circles in Figs. 4,Ic, 4,Id). The closer to the array the focus was steered, the lower source pressure amplitude p_0 was required for the shock to be formed in the grating lobe. At the 10%-pressure drop steering limit (Fig. 4,Id, $\Delta z = -19.5$ mm), shock formation in the grating lobe was achieved at even lower source pressure amplitude (red circles) compared to the shock wave formation in the main focus (red x-symbols). At both prefocal steering distances, however, shock amplitudes in the grating lobe were 40–70% lower than those in the main focal lobe (Figs. 4,Ic–4,Id), including fully developed shock regimes at the focus (Fig. 4,If). The maximum prefocal steering distance, at which the grating lobe did not form within the double focal distance range was found to be $\Delta z = -4$ mm (data not shown).

Postfocal steering effects in nonlinear array field. When steering postfocally to the 10%-pressure drop limit ($\Delta z = 7.5$ mm, green curves in Fig. 4,II), a fully developed shock formed at the focus at slightly higher source pressure amplitude p_0 (by 7%) as compared to the no steering case (squares in Fig. 4,IIb). This may seemingly contradict the pattern typical for weaker-focusing single-element transducers [12], however it was also observed by Bawiec et al. (2021) [18] for a 256-element therapeutic array due to the drop in focal pressure amplitude when steering postfocally (Fig. 3c). In contrast to the prefocal steering, here the peak positive pressure in the grating lobe was always lower than that in the main lobe regardless of the source pressure amplitude p_0 (solid curves in Figs. 4,IIc, 4,IId). Peak negative pressure in the grating lobe, however, exceeded that in the main lobe above $p_0 = 0.45$ MPa when the focus was steered postfocally (dashed curve in Fig. 4,IId). Again, in contrast to prefocal steering, no shocks were formed in the grating lobe regardless of the considered source pressure amplitude p_0: neither at the maximum ratio of the peak positive pressure in the grating *vs* main lobe (triangles in Figs. 4,IIc, 4,IId; 4,IIe), nor in the fully developed shock regime at the focus (squares in Figs. 4,IIb–4,IId; 4,IIf).

2.3. Decreasing Focusing Angle: Electronic vs Geometric

Figure 5,I compares the two approaches aimed to decrease the focusing angle from 77° down to 71°: postfocal electronic focus steering of the fully operating array (blue) *vs* geometric setting of the angle by switching off the two outer rings of the array (red).

Figures 5,Ib–5,Id illustrate the effects of the two approaches on the linear fields produced. At the same source pressure amplitude, the ten-ring configuration generated a focal lobe of the same dimensions as did the full array with electronic focus steering (Figs. 5,Ic–5,Id; Table 1), with 8% lower focusing gain G (Fig. 5,Ib; Table 1). The lower focusing gain was apparently accounted for by a combined effect of 17% decrease in the active surface area of the array with the two rings switched off (Table 1) and 10% drop in focal pressure amplitude for the full array due to postfocal steering (Fig. 3c). At the same source power, in linear regime the ten-ring configuration produced the same peak pressure in the main lobe (data not shown). Ratio of the grating *vs* main lobe pressure amplitude was noticeably lower for the ten-ring configuration without focus steering as compared to the full array case, 31 *vs* 58% (Fig. 5,Ib).

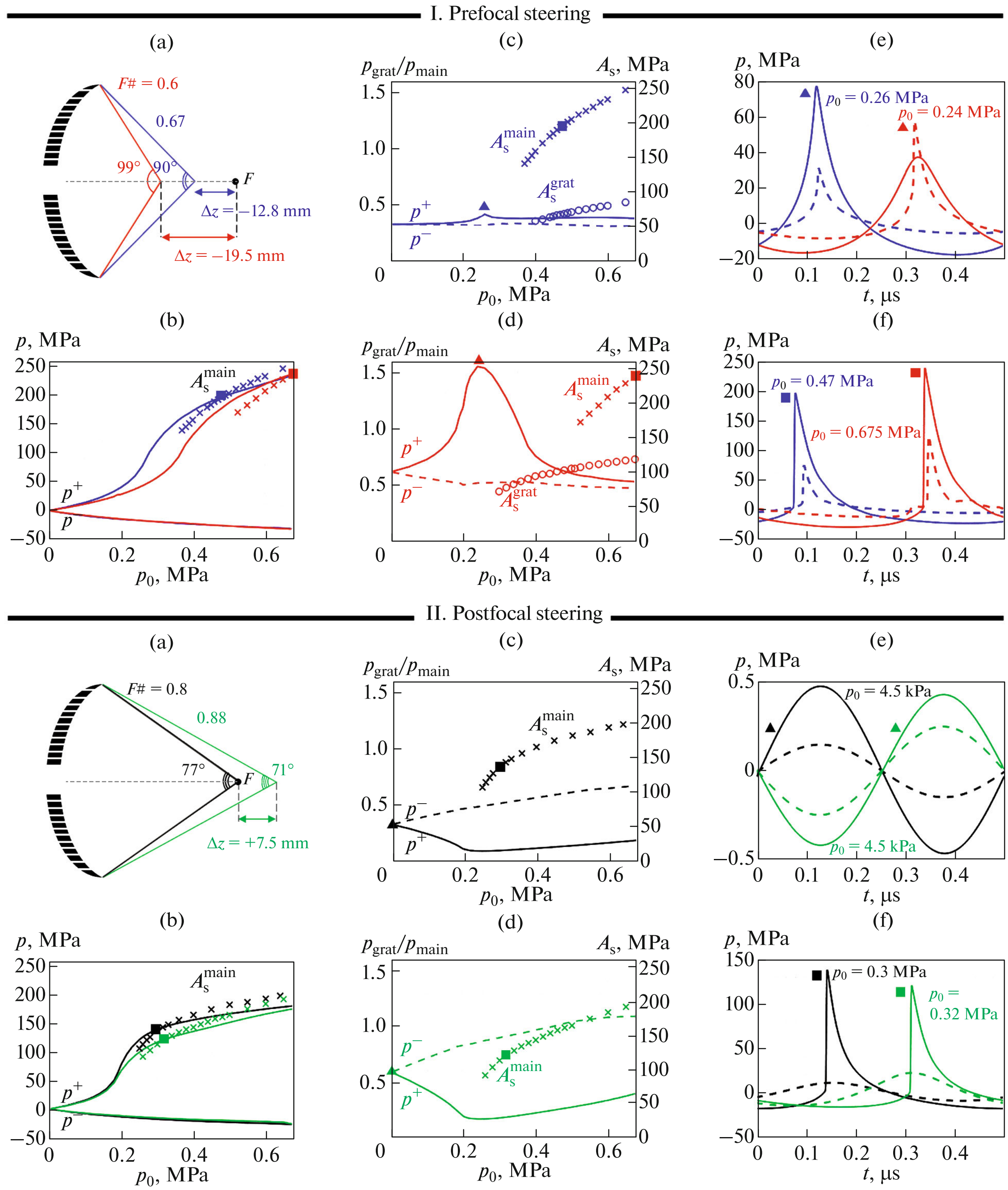

Fig. 4. Illustration of the focus steering effect on nonlinear field of the annular array with all rings enabled: (I) prefocal steering, (II) postfocal steering. The colors correspond to the limiting steering distances from Fig. 3: prefocal (blue) and postfocal (black) thermally safe limits; prefocal (red) and postfocal (green) 10%-pressure drop limits. (a) Schematics of the annular array with varied electronically steered focus positions relative to the geometric focus *F*. (b) Nonlinear saturation curves for peak positive (p+) and negative (p–) focal pressures (solid lines) and shock amplitude at the steered focus (x-symbols) as functions of the source pressure amplitude p_0. (c)–(d) Ratio of peak positive (p+, solid line) and negative (p–, dashed line) pressures in the grating lobe *vs* in the main lobe, and shock amplitudes in the main lobe (A_s^{main}, x-symbols) and in the grating lobe (A_s^{grat}, circles) as functions of source pressure amplitude p_0. Left vertical axis shows the pressure ratio, right vertical axis shows the shock amplitude. (e)–(f) Pressure waveforms in the main (solid line) and grating (dashed line) lobes at p_0 value corresponding to: (e)—the maximum ratio of peak positive pressure at the grating *vs* at the main lobe peak (triangles in (c),(d)); (f)—fully developed shock formation in the main lobe (squares in (b)–(d)). The waveforms are shifted in time for better separation on the graphs.

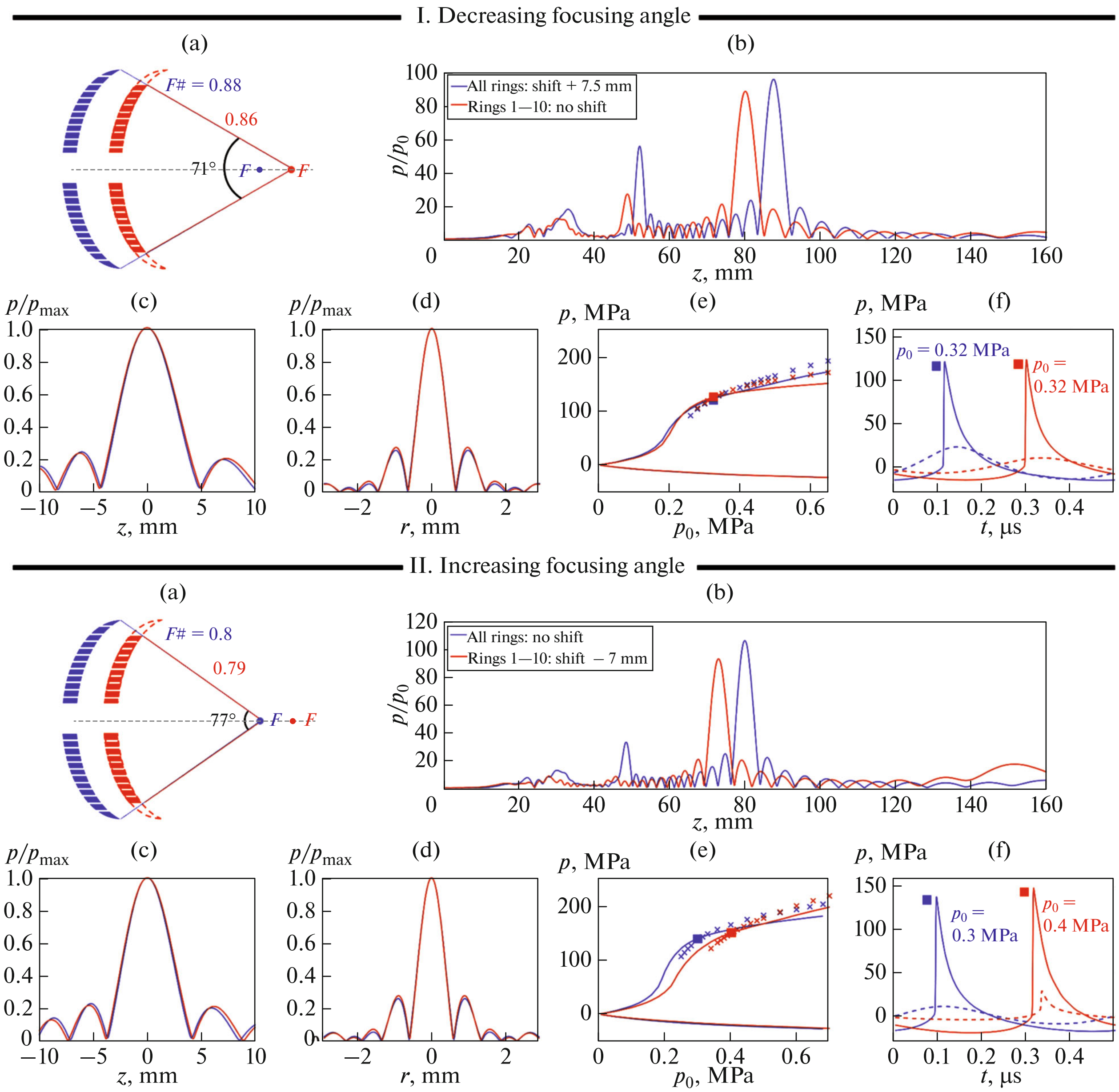

Fig. 5. Illustration of effects of electronic *vs* geometric decreasing (I) and increasing (II) of the annular array focusing angle. (a) Schematics of the annular array configurations: all twelve (blue) or ten (red) rings enabled, with varied electronically steered focus position relative to the geometric focus *F*. (b) Axial pressure amplitude distributions relative to the source pressure amplitude p_0 in a linear regime. (c)–(d) Normalized peak positive pressure distributions in a linear regime in the neighborhood of the maximum pressure point (0): (c) axial and (d) transverse. (e) Nonlinear saturation curves for peak positive (p+) and negative (p–) focal pressures (solid lines) and shock amplitude at the focus (x-symbols) as functions of the source pressure amplitude p_0. (f) Pressure waveforms in the main (solid line) and grating (dashed line) lobes at p_0 value corresponding to the developed shock formation in the main lobe (squares in (e)).

Figures 5,Ie–5,If illustrate the effects that the two considered approaches had on the produced nonlinear fields. As expected from the results obtained for postfocal steering (Fig. 4,IIb), a fully developed shock formed in the main lobe at the same source pressure amplitude $p_0 = 0.32$ MPa in both cases (i.e., at a lower source power for the ten-ring case), with a slightly higher shock amplitude in the ten-ring configuration (squares in Figs. 5,Ie–5,If; Table 1). Nonlinear saturation in the case of the ten-ring array, however, was reached at a lower peak positive pressure. Figure 5,If also demonstrates almost sinusoidal behavior of the waveforms at the grating lobe peak (dashed lines) when a fully developed shock was formed in the main lobe (solid lines) in both configurations (squares in Fig. 5,Ie).

2.4. *Increasing Focusing Angle: Electronic vs Geometric*

Figure 5,II compares the two approaches to set the focusing angle to 77°: geometric setting of the angle by enabling all rings of the array (blue) *vs* prefocal electronic steering of the ten-ring array (red). The latter configuration produced the focal lobe of the same dimensions as the full array (Figs. 5,IIc–5,IId; Table 1) with 12% lower focusing gain (Fig. 5,IIb; Table 1). This can be accounted for by a 17% decrease in the active surface area for a ten-ring array (Table 1) outweighing a 5% pressure gain due to prefocal steering (Fig. 3c). At the same source power, in linear regime the ten-ring array with prefocal electronic steering produced only 4% lower peak positive pressure as compared to the full array (data not shown). As expected from Fig. 4,I for prefocal steering, a postfocal grating lobe was formed in the linear field of the ten-ring array with prefocally steered focus (Fig. 5,IIb), with apparent nonlinear distortion of the waveform at higher p_0 in the grating lobe (red dashed curve in Fig. 5,IIf), which was not observed for the full array with no focus steering (blue dashed curve in Fig. 5,IIf). Surprisingly for the beams with the same focusing angle, a fully developed shock A_s^{dev} of a 9% higher amplitude was formed in the main lobe at a 33% higher source pressure amplitude p_0^{dev} (or, 22% higher power, considering active surface ratio) in the ten-ring case (squares in Fig. 5,IIe; Table 1), which can be accounted for by a 12% lower focusing gain in this case (Fig. 5,IIb; Table 1).

DISCUSSION AND CONCLUSIONS

In this paper, a set of multiparametric acoustic field simulations was performed to investigate the effects of electronic *vs* geometric adjustment of an annular array focusing angle on the produced linear and nonlinear fields. An example of the 12-element annular array used in laboratory experiments was considered [19, 20]. It was shown that relatively large width of the array elements resulted in formation of a strong prefocal sidelobe even without focus steering and thus almost negligible capability of the array for postfocal steering without exceeding a thermally safe limit. However, for applications that rely on nonlinear effects and presence of shocks, the thermally safe limit, introduced for the linear beam focusing, can be exceeded as nonlinear effects were shown to be weak in the prefocal lobe. Focusing postfocally to the 10%-pressure drop distance (i.e., +7.5 mm from the geometric focus) resulted in 11% decrease in the amplitude of the developed shock, which formed with a small power compensation. However, shock-induced absorption or radiation force, which are proportional to the shock amplitude cubed, would be 30% lower than those in the case without steering.

The range of prefocal steering was shown to be much larger as compared to postfocal, which was 12.8 and 19.5 mm for the thermally safe and 10%-pressure drop limits, respectively. However, the amplitude of the developed shock, corresponding power requirements, and absorption rates changed significantly with steering. Compared to the case with no steering, when steering prefocally to 12.8 and 19.5 mm from the geometric focus, developed shocks formed at 2.45- and 5-times higher power level, had 42 and 74% higher amplitude, which would result in 2.9- and 5.3-times higher absorption rate or radiation force, respectively. This should be taken into account to equalize thermal, mechanical, or pushing effects of nonlinear ultrasound waves when developing exposure protocols with electronic focus steering. In addition, prefocal axial steering of the focus was shown to result in formation of the shock in a postfocal grating lobe at even lower array power than that required for shock formation in the main lobe. However, simulations here were performed in water and even in this case the obtained shock amplitude in the grating lobe was significantly smaller than that in the main lobe. Absorption in soft tissues and corresponding wave attenuation with the propagation distance would suppress shock formation in the postfocal field.

General nonlinear effects observed for electronic focus steering were compared to the well-studied cases of the geometric adjustment of the focusing angle [10, 11]. To decrease the focusing angle, geometric approach (i.e., switching off the two outer rings of the array) resulted in formation of a focal lobe of the same dimensions as compared to the postfocal electronic steering approach, a lower-level prefocal grating lobe, and a fully developed shock forming only in the main lobe at the same source pressure amplitude and having slightly higher amplitude. Taking into account a lower amplitude of the prefocal grating lobe, switching off the outer rings of the annular array, therefore, should be considered more suitable for decreasing the focusing angle as compared to the postfocal electronic steering of the full array.

Increasing focusing angle was achieved by prefocal steering of the ten-ring array focus, and the resulting field was compared to that of the full array with the same focusing angle. In agreement with the results above, prefocal steering of the ten-ring array focus resulted in formation of a postfocal grating lobe that may contain low-amplitude shock waves. Geometric approach allowing to avoid prefocal steering, therefore, was found to be more suitable for increasing the focusing angle, however electronic steering approach may be feasible in absorptive propagation media that could suppress postfocal shock formation.

In conclusion, in further use of the array in laboratory experiments studying shock-wave-based applications that require exposures along the array axis and specified minimal amplitude of the developed shock at the focus, the following procedure can be used. First, several outer elements should be turned off to match the corresponding focusing angle of the beam without electronic focus steering. This would minimize the effect of side lobes. Next, the acoustic power required for the formation of the developed shock at the main focus should be estimated, and then at least 20% higher power should be used to reach the smooth part of the saturation curve. The steering range at least from −12.5 to +7.5 mm from the geometric focus (20 mm total) is feasible with additional up to twofold power compensation when steering prefocally. Alternatively, the same high power can be used for all steering positions.

FUNDING

The study was supported in parts by the Russian Science Foundation (projects no. 20-12-00145 and 22-22-00751), student stipends from BASIS Foundation (projects no. 20-2-10-10-1 and 22-2-1-28-1) and was performed within the frame of the Interdisciplinary Scientific and Educational School of Moscow University "Photonic and Quantum technologies. Digital medicine".

CONFLICT OF INTEREST

The authors declare that they have no conflicts of interest.

REFERENCES

1. G. T. Haar and C. Coussios, Int. J. Hyperthermia **23** (2), 89 (2007). https://doi.org/10.1080/02656730601186138
2. F. Wu, W. Zhi-Biao, C. Wen-Zhi, Z. Hui, B. Jin, Z. Jian-Zhong, L. Ke-Quan, J. Cheng-Bing, X. Fang-Lin, and S. Hai-Bing, Ann. Surg. Oncol. **11**, 1061 (2004). https://doi.org/10.1245/ASO.2004.02.026
3. G. K. Hesley, K. R. Gorny, T. L. Henrichsen, D. A. Woodrum, and D. L. Brown, Ultrasound Q. **24** (2), 131 (2008). https://doi.org/10.1097/RUQ.0b013e31817c5e0c
4. Z. Xu, T. L. Hall, E. Vlaisavljevich, and F. T. Lee, Jr., Int. J. Hyperthermia **38** (1), 561 (2021). https://doi.org/10.1080/02656736.2021.1905189
5. M. S. Canney, V. A. Khokhlova, O. V. Bessonova, M. R. Bailey, and L. A. Crum, Ultrasound Med. Biol. **36** (2), 250 (2010). https://doi.org/10.1016/j.ultrasmedbio.2009.09.010
6. T. D. Khokhlova, M. S. Canney, V. A. Khokhlova, O. A. Sapozhnikov, L. A. Crum, and M. R. Bailey, J. Acoust. Soc. Am. **130** (5), 3498 (2011). https://doi.org/10.1121/1.3626152
7. A. Maxwell, O. Sapozhnikov, M. Bailey, L. Crum, Z. Xu, B. Fowlkes, C. Cain, and V. Khokhlova, Acoust. Today **8** (4), 24 (2012). https://doi.org/10.1121/1.4788649
8. Y. A. Pishchalnikov, O. A. Sapozhnikov, and T. V. Sinilo, Acoust. Phys. **48** (2), 214 (2002). https://doi.org/10.1134/1.1460959
9. A. P. Sarvazyan, O. V. Rudenko, and M. Fatemi, IEEE Trans. Ultrason. Ferroelectr. Freq. Control. **68** (11), 3261 (2021). https://doi.org/10.1109/TUFFC.2021.3112505
10. P. B. Rosnitskiy, P. V. Yuldashev, and V. A. Khokhlova. Acoust. Phys. **61** (3), 301 (2015). https://doi.org/10.1134/S1063771015030148
11. P. B. Rosnitskiy, P. V. Yuldashev, O. A. Sapozhnikov, A. D. Maxwell, W. Kreider, M. R. Bailey, and V. A. Khokhlova, IEEE Trans. Ultrason. Ferroelectr. Freq. Control **62** (2), 374 (2017). https://doi.org/10.1109/TUFFC.2016.2619913
12. T. Khokhlova, P. Rosnitskiy, C. Hunter, A. Maxwell, W. Kreider, G. Ter Haar, M. Costa, O. Sapozhnikov, and V. Khokhlova, J. Acoust. Soc. Am. **144** (3), 1160 (2018). https://doi.org/10.1121/1.5052260
13. L. R. Gavrilov and J. A. Hand, IEEE Trans. Ultrason. Ferroelectr. Freq. Control **47** (1), 125 (2000). https://doi.org/10.1109/58.818755
14. S. A. Ilyin, L. R. Gavrilov, and V. A. Khokhlova, Mem. Fac. Phys. **5**, 342 (2014).
15. K. Hynynen and R. M. Jones, Phys. Med. Biol. **61** (17), 206 (2016). https://doi.org/10.1088/0031-9155/61/17/R206
16. M. Wang and Y. Zhou, Int. J. Hyperthermia **33** (7), 758 (2017). https://doi.org/10.1080/02656736.2017.1309579
17. M. Wang and Y. Zhou, Int. J. Hyperthermia **32** (5), 569 (2016). https://doi.org/10.3109/02656736.2016.1160154
18. C. R. Bawiec, T. D. Khokhlova, O. A. Sapozhnikov, P. B. Rosnitskiy, B. W. Cunitz, M. A. Ghanem, C. Hunter, W. Kreider, G. R. Schade, P. V. Yuldashev, and V. A. Khokhlova, IEEE Trans. Ultrason. Ferroelectr. Freq. Control **68** (5), 1496 (2021). https://doi.org/10.1109/TUFFC.2020.3036580
19. A. Z. Kaloev, D. A. Nikolaev, V. A. Khokhlova, S. A. Tsysar, and O. A. Sapozhnikov, Acoust. Phys. **68** (1), 71 (2022). https://doi.org/10.1134/S1063771022010043
20. E. M. Ponomarchuk, P. B. Rosnitskiy, S. A. Tsysar, T. D. Khokhlova, M. M. Karzova, A. V. Tyurina, K. D. Tumanova, A. V. Kadrev, S. V. Buravkov, P. E. Trakhtman, N. N. Starostin, O. A. Sapozhnikov, and V. A. Khokhlova, J. Acoust. Soc. Am. **150** (4), A84 (2021). https://doi.org/10.1121/10.0007706
21. P. V. Yuldashev, I. S. Mezdrokhin, and V. A. Khokhlova, Acoust. Phys. **64** (3), 309 (2018). https://doi.org/10.1134/S1063771018030168
22. P. V. Yuldashev, M. M. Karzova, W. Kreider, P. B. Rosnitskiy, O. A. Sapozhnikov, and V. A. Khokhlova, IEEE Trans. Ultrason. Ferroelectr. Freq. Control **68** (9), 2837 (2021). https://doi.org/10.1109/TUFFC.2021.3074611

23. V. A. Khokhlova, P. V. Yuldashev, I. Mezdrokhin, P. Rosnitskiy, M. M. Karzova, W. Kreider, and O. Sapozhnikov, J. Acoust. Soc. Am. **144** (3), 1699 (2018).
https://doi.org/10.1121/1.5067551

24. https://limu.msu.ru/node/3555?language=en.

25. F. Duck, *Physical Properties of Tissue: a Comprehensive Reference Book* (Academic, London, 1990).

26. N. T. O'Neil, J. Acoust. Soc. Am. **21** (5), 516 (1949).

27. D. Cathignol and O. A. Sapozhnikov, Acoust. Phys. **45** (6), 735 (1999).
https://doi.org/10.1134/S1063771018030168

28. E. S. Ebbini and C. A. Cain, IEEE Trans. Biomed. Eng. **38** (7), 634 (1991).
https://doi.org/10.1109/10.83562

29. S. A. Ilyin, P. V. Yuldashev, V. A. Khokhlova, L. R. Gavrilov, P. B. Rosnitskiy, and O. A. Sapozhnikov, Acoust. Phys. **61** (1), 52 (2015).
https://doi.org/10.1134/S1063771015010042

30. M. Averiyanov, S. Ollivier, V. Khokhlova, and Ph. Blanc-Benon, J. Acoust. Soc. Am. **130** (6), 3595 (2011).
https://doi.org/10.1121/1.3652869

31. C. Perez, H. Chen, T. J. Matula, M. M. Karzova, and V. A. Khokhlova, J. Acoust. Soc. Am. **134** (2), 1663 (2013).
https://doi.org/10.1121/1.4812885